Strain-Induced Crystallization and Mechanical Properties of Functionalized Graphene Sheet-Filled Natural Rubber

Bulent Ozbas,[1]* Shigeyuki Toki,[2] Benjamin S. Hsiao,[2] Benjamin Chu,[2] Richard A. Register,[1] Ilhan A. Aksay,[1] Robert K. Prud'homme,[1] Douglas H. Adamson[3,4]

[1]Department of Chemical and Biological Engineering, Princeton University, Princeton, New Jersey 08544

[2]Department of Chemistry, State University of New York, Stony Brook, New York 11794

[3]Institute of Materials Science, Polymer Program, University of Connecticut, Storrs, Connecticut 06269

[4]Department of Chemistry, University of Connecticut, Storrs, Connecticut 06269

Correspondence to: R. K. Prud'homme (E-mail: prudhomm@princeton.edu) or D. H. Adamson (E-mail: adamson@uconn.edu)

Received 14 February 2012; accepted 15 February 2012; published online 11 March 2012
DOI: 10.1002/polb.23060

ABSTRACT: The effects of functionalized graphene sheets (FGSs) on the mechanical properties and strain-induced crystallization of natural rubber (NR) are investigated. FGSs are predominantly single sheets of graphene with a lateral size of several hundreds of nanometers and a thickness of 1.5 nm. The effect of FGS and that of carbon black (CB) on the strain-induced crystallization of NR is compared by coupled tensile tests and X-ray diffraction experiments. Synchrotron X-ray scattering enables simultaneous measurements of stress and crystallization of NR in real time during sample stretching. The onset of crystallization occurs at significantly lower strains for FGS-filled NR samples compared with CB-filled NR, even at low loadings. Neat-NR exhibits strain-induced crystallization around a strain of 2.25, while incorporation of 1 and 4 wt % FGS shifts the crystallization to strains of 1.25 and 0.75, respectively. In contrast, loadings of 16 wt % CB do not significantly shift the critical strain for crystallization. Two-dimensional (2D) wide angle X-ray scattering patterns show minor polymer chain alignment during stretching, in accord with previous results for NR. Small angle X-ray scattering shows that FGS is aligned in the stretching direction, whereas CB does not show alignment or anisotropy. The mechanical properties of filled NR samples are investigated using cyclic tensile and dynamic mechanical measurements above and below the glass transition of NR. © 2012 Wiley Periodicals, Inc. J Polym Sci Part B: Polym Phys 50: 718–723, 2012

KEYWORDS: composites; crystallization; graphene; rubber; WAXS

INTRODUCTION Natural rubber (NR) is a remarkable material that, when crosslinked, can be stretched to strains over 700% without rupture. At these high strains, rubber becomes "self-reinforcing", that is, it microcrystallizes, and the mechanical properties increase. In most applications of NR, fillers are added to increase modulus and toughness, with the most common filler being carbon black (CB),[1,2] comprising ~20-nm primary particles aggregated in fractal structures with surface areas of ~80 m^2/g. We have previously developed functionalized graphene sheet (FGS) nanofillers[3,4] with surface chemistries similar to CB, but with thicknesses on the atomic scale, in-plane dimensions on the order of 100–1000 nm, and nitrogen adsorption surface areas of 500–700 m^2/g. The high aspect ratio and electrical conductivity of FGS makes it of interest as a nanofiller to impart mechanical strength, electrical conductivity, and barrier properties to elastomers.[5–7]

In this article, the effect of FGS on the crystallization and mechanical properties of NR is investigated. By comparing CB- and FGS-filled NR, we can begin to address questions concerning the mechanism of strain-induced crystallization in NR. Crystallization and mechanical reinforcement of filled NR is variously attributed to "strain amplification" and "stress transmission" through the filler network.[8–10] FGS has an aspect ratio of more than 400, much larger than the 5–10 aspect ratio of CB. This provides a second length scale on which strain-induced crystallization may depend. Furthermore, We use high-strain and low-strain mechanical measurements, synchrotron X-ray scattering, and measurements above and below the glass transition temperature to shed light on the mechanism of reinforcement and strain-induced crystallization of NR by FGS.

The preparation of single-sheet graphene nanofillers is achieved by exfoliation of natural flake graphite by a process involving oxidation and rapid heating.[3,4] AFM images[4] reveal that over 80% of the graphene flakes are single sheets with an average lateral size of 400 nm. The exfoliated material has an atomic carbon:oxygen ratio (C/O) of ~12 with the

Additional Supporting Information may be found in the online version of this article.
Present address: Bulent Ozbas, Air Products and Chemicals, Inc., 7201 Hamilton Boulevard, Allentown, Pennsylvania 18195.

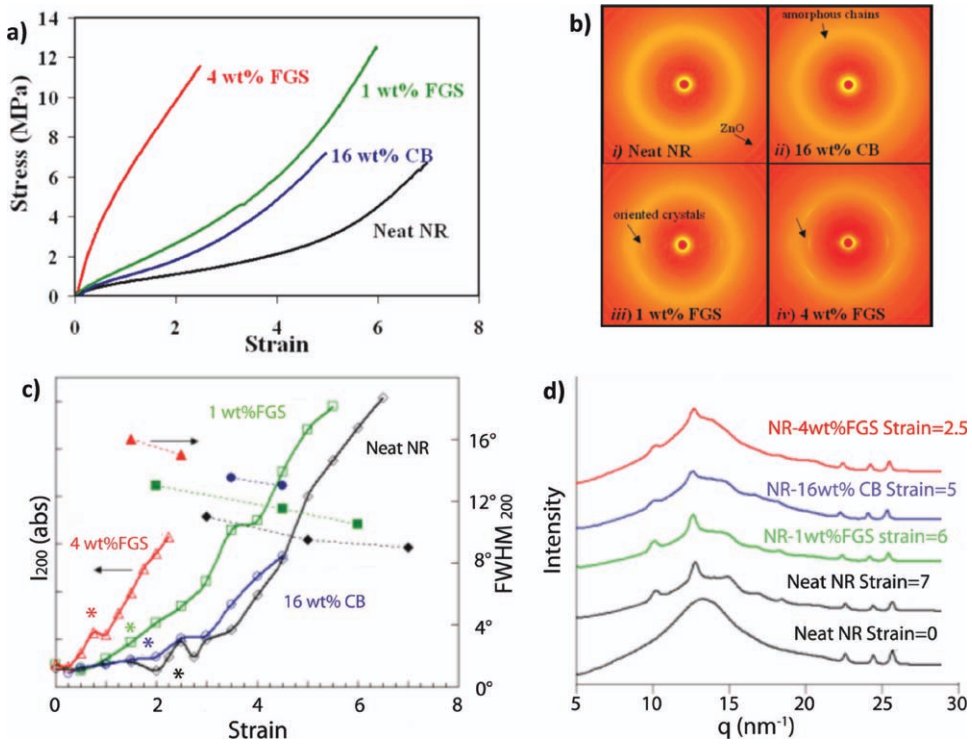

FIGURE 1 Coupled WAXD and tensile tests for neat NR and NR filled with 1 and 4 wt % FGS, and 16 wt % CB. (a) Engineering stress versus strain. (b) 2D WAXD patterns at strain = 2 (air scattering is subtracted as background). Stretch direction is vertical. (c) Integrated intensity (open symbols, left axis) and azimuthal breadth (FWHM, filled symbols, right axis) for the NR 2 0 0 reflection versus strain. Asterisks represent the onset of crystallization, as detected by a visible 200 arc on the equator. (d) 1D WAXD patterns for unstretched neat NR, and all samples shortly before failure in the tensile test. Small peaks from 22 to 26 nm^{-1} are from ZnO in the base rubber formulations.

oxygenated species expected to be primarily hydroxyl and epoxy moieties.[11,12] The polar functional groups enable facile dispersion in NR and should provide comparable coupling of the polymer matrix to the FGS during crosslinking as is observed for CB.

Strain-induced crystallization at large elongations (>300% strain) plays a major role in the mechanical properties of NR.[13–15] When the strain-induced crystallization of NR is suppressed at elevated temperatures, the tensile strength drops dramatically.[16,17] Recently, it has been possible to measure the extent of crystallization of NR during tensile deformation using real time synchrotron X-ray diffraction and NMR.[18–21] Using synchrotron diffraction, Toki et al. showed that the majority of the chains (~75% by mass) remain amorphous and unoriented even at large deformations because of the inhomogeneities in the crosslinked network.[20] Although the crosslinking density did not alter the onset of crystallization in NR,[19] it could be affected by filler content.[13,16,22] The effective filler volume fraction includes immobilized rubber, which is restrained on the particle surface because of attractive interactions between the filler and polymer chains. This layer exhibits slow dynamics and thus becomes energetically distinguishable from the matrix regions that are away from the filler surface.[23] The amount of immobilized rubber depends on several factors, including the particle size, aggregate structure, and surface chemistry.[24–30] In this work, we present parallel small angle X-ray scattering (SAXS), wide angle X-ray scattering, and tensile measurements on CB and FGS composites to elucidate the mechanisms of FGS nanofiller reinforcement of NR.

RESULTS AND DISCUSSION

Figure 1 shows the coupled X-ray diffraction and tensile test data for neat and filled NR samples. These data allow correlation of the measured stress to the onset of crystallization, degree of crystallinity, and orientation of the crystallites. The tensile tests in Figure 1(a) show that, with only 1 wt % FGS, higher modulus and strength are obtained when compared with NR containing 16 wt % CB. With 4 wt % FGS loading, the Young's modulus increases by 600%, the modulus at strain $\varepsilon = 1$ by 700%, and strength by 75%. However, the elongation at break decreases with both FGS and CB loading. In Figure 1(b), examples of 2D wide angle X-ray diffraction (WAXD) patterns of neat NR and NR filled with 16 wt % CB and 1 and 4 wt % FGS are shown for a strain $\varepsilon = 2$. The halo at $q \sim 13$ nm^{-1} is due to scattering from amorphous chains, corresponding to ~80% of all scattering intensity even at $\varepsilon = 7$ for neat NR. At $\varepsilon = 2$, narrow arcs from rubber crystallites become apparent in the 1 and 4 wt % FGS-NR composites, whereas for neat and 16 wt % CB in NR,

TABLE 1 Comparison of Onset of Crystallization Values for Neat and, CB- and FGS-Filled NR Samples

	Onset of Crystallization, Strain[b]		
Samples[a]	This Study	Ref. 22	Ref. 33
Neat NR	2.25	2.0	3
16 wt % CB (20 phr CB)	1.75	1.6	
27 wt % CB (40 phr CB)		1.3	
33 wt % CB (50 phr CB)			1
1 wt % FGS	1.25		
4 wt % FGS	0.75		

[a] In Refs. 22 and 33, the CB content is given as phr. These values are converted to wt % using the reported formulations.
[b] In Refs. 22 and 33, onset of crystallization values are reported as extension ratio, and they are converted to strain. They are determined by X-ray diffraction experiments.

crystallization is still not observed. The sharp intensity increase for the 2 0 0 reflection ($q = 10.3$ nm^{-1}) on the equator for FGS nanocomposites reveals that the crystallites are oriented as they form, with the crystallite normals along the stretching direction. The crystallization of NR is followed by the change in the intensity of the 2 0 0 reflection calculated by integrating over $9.6 < q < 11.0$ nm^{-1} and $70^\circ < \varphi < 110^\circ$, where φ is the azimuthal angle relative to the meridian. Figure 1(c) shows that neat NR exhibits two distinct regimes for the 2 0 0 reflection. For $\varepsilon < 2$, the change in scattering intensity is not significant, whereas for $\varepsilon > 4$, the intensity increases sharply and almost linearly. This behavior reflects the onset of crystallization.[20,31,32] For neat NR, the complete φ scans show that the 2 0 0 reflection at the equator starts to appear at $\varepsilon = 2.25$, which is marked as the onset of crystallization. Figure 1(c) shows that the onset and progression of crystallization for NR containing 16 wt % CB are essentially the same as those for neat NR. Similar values for the onset of crystallization in neat and CB-filled NR have been reported by others.[22,33] Table 1 shows the reported strain at the onset of crystallization for neat and CB-filled NR measured by WAXD. The FGS-filled samples show a dramatic decrease in strain values at the onset of crystallization. The 1 wt % FGS-NR sample shows an onset of crystallization at $\varepsilon = 1.25$, whereas the onset of crystallization for 4 wt % FGS-NR is at $\varepsilon = 0.25$. In contrast, it requires 27 wt % [40 parts per hundred of rubber (phr)] CB to initiate NR crystallization at $\varepsilon = 0.25$.[22]

One can estimate the effective volume fraction (ϕ') of filler in rubber using $\phi' = (\alpha_{neat} - \alpha_{filled})/(\alpha_{neat} - 1)$, where α_{neat} and α_{filled} are the macroscopic extension ratios ($\alpha = \varepsilon + 1$) for the neat and filled samples, respectively.[16,27,34] This equation relates the global strain (ε) to the amplified local strain of the chains because of the presence of stiff particles—the "strain amplification" explanation of the early onset of crystallization.[4] It is reasonable to assume that, at the molecular level, rubber crystallization starts in the filled NR matrix at the same average local strain at which it occurs in neat NR, that is, $\varepsilon = 2.25$. Then for 16 wt % CB with a volume fraction $\phi \sim 0.1$, the effective volume fraction can be calculated as $\phi' = 0.22$. For CB, the effective volume fraction is double the filler volume fraction, ϕ. On the other hand, for only 1 wt % FGS (i.e., $\phi \sim 0.005$) $\phi' = 0.44$—the effective volume fraction is 90 times the actual volume fraction of filler. For 4 wt % FGS, $\phi \sim 0.02$ with $\phi' = 0.67$—30 times the actual value. This demonstrates the ability of the high aspect ratio FGS to produce locally high strain in the rubber matrix.

It has been proposed that "immobilized rubber" contributes to the effective volume fraction of the filler and thereby increases the modulus.[8,9] This would suggest that the volume fraction increase should scale with the surface area of the filler. The CB used in this study has a Brunauer–Emmett–Teller surface area of 80 m^2/g, whereas FGS has a surface area of ~600 m^2/g. Arguing that the surface chemistry is similar, the amount of immobilized rubber in a FGS-filled rubber is expected to be 7–8 times more than in an analogous CB-filled one. This value can be considered as a first estimate of the relative amounts of immobilized rubber; the surface areas are measured by nitrogen adsorption, but 20% of the measured surface area of N330 CB is due to micropores[1] with diameter less than 2 nm, which are not available for polymer adsorption. Yet, it is obvious that the 7- to 8-fold increase in immobilized rubber volume fraction cannot account for the 30- to 90-fold increase in the effective volume fraction observed from the decrease in the strain to initiate crystallization.

Although FGS induces crystallization at much lower global strains than CB-filled NR or neat NR, the degree of crystallinity at maximum extension is essentially the same for all samples. Figure 1(d) shows the integrated 1D scattering plot for all samples at strain values before catastrophic failure. When the 1D WAXD patterns are fit to a series of crystalline and amorphous peaks, the contribution of the total intensity from all crystalline reflections is found to be between 10 and 15% of the total scattering intensity for all the samples, suggesting similar crystallinity at maximum extension.

Earlier studies of strain-induced crystallization in NR showed that the orientation of crystals along the stretching direction is partially disrupted by the presence of CB.[16] Figure 1(c) shows the azimuthal breadth of the 2 0 0 reflections (full width at half maximum, FWHM) for neat and filled samples at their largest elongation. Azimuthal peak breadths, representing the distribution of crystallite orientations, increase for filled systems. Interestingly, the azimuthal breadth for the 1 wt % FGS-filled NR is smaller than that for 16 wt % CB-filled NR, despite the fact that the former exhibited a crystallization onset at lower strain. This behavior can be attributed to topological differences between FGS and CB. The crystallite dimensions in rubber are tens of nanometers in size[35] and are comparable to the particle size of spherical CB particles. However, FGS nanosheets have lateral dimensions on the order of hundreds of nanometers and are aligned in the stretching direction during deformation as shown in the following section. Therefore, the crystal orientation is biased in the direction of stretching.

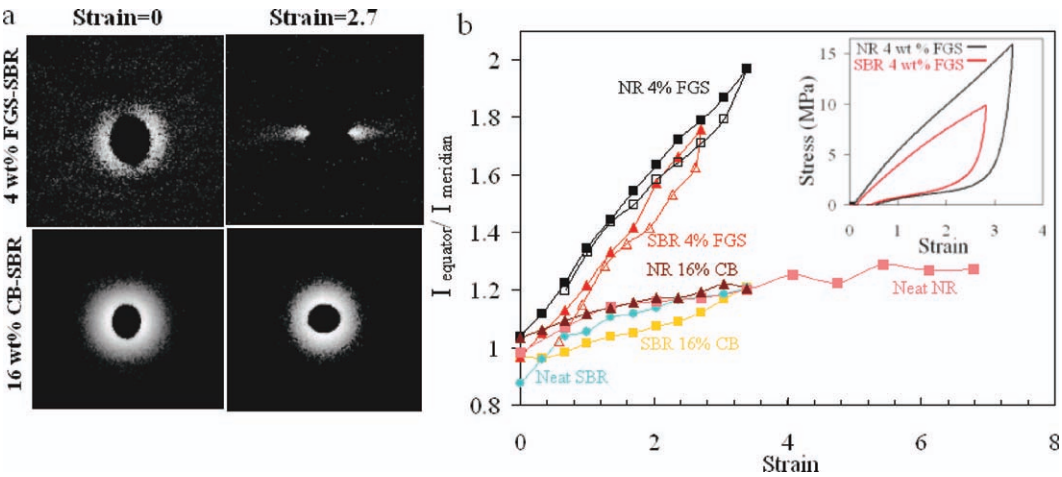

FIGURE 2 Coupled SAXS and tensile tests for neat NR, neat SBR, 16 wt % CB-filled NR and SBR, and 4 wt % FGS-filled NR and SBR. (a) 2D SAXS patterns for 4 wt % FGS and 16 wt % CB-filled SBR at strain = 0 and strain = 2.7. (b) The ratio of scattering intensities integrated at the equator and meridian versus strain. For FGS-filled SBR and NR samples retraction curves are also plotted. Inset: Stretching and retraction data for 4 wt % FGS-filled SBR and NR.

Although FGS is randomly dispersed in undeformed NR samples, the plate-like structures can be aligned in the stretching direction, especially at large elongations. The alignment of FGS in the stretching direction is expected to significantly contribute to the mechanical properties of the nanocomposites because of the higher in-plane modulus relative to the bending modulus of a graphene sheet. The stiffening of the composite due to alignment is not expected in isotropic fillers such as CB and fume silica. To show alignment, the orientation of FGS in rubber matrices during extension was studied by time-resolved SAXS measurements. Figure 2(b) shows the results for NR and styrene–butadiene rubber (SBR) filled with FGS and CB. SBR does not exhibit strain-induced crystallization, and thus, there is no intensity increase on the equator for the unfilled polymer. For FGS-filled samples, the ratio of the intensity at the equator (I_{90°) to the intensity at the meridian (I_{0°) becomes larger during stretching. Examples of 2D patterns are given for FGS- and CB-filled SBR at strains of $\varepsilon = 2.7$ in Figure 2(a). While the contribution of CB to the scattering is isotropic, FGS-filled samples form streaks on the equator when stretched, indicating that FGS are aligned parallel to the stretching direction. In previous studies, it has been shown that FGS is not flat; rather, it has a wrinkled structure.[3] The effect of this wrinkling on the bending modulus of the fillers is under investigation. The alignment of FGS is also shown to be reversible in Figure 2(b); the I_{90°/I_{0° values are nearly superimposable for extension and retraction for FGS-filled samples.

Dynamic mechanical results are shown in Figure 3. At room temperature, NR filled with 4 wt % FGS or 16 wt % CB shows E' (storage modulus) values 13.4 and 2.6 times higher, respectively, than neat NR. However, below the glass

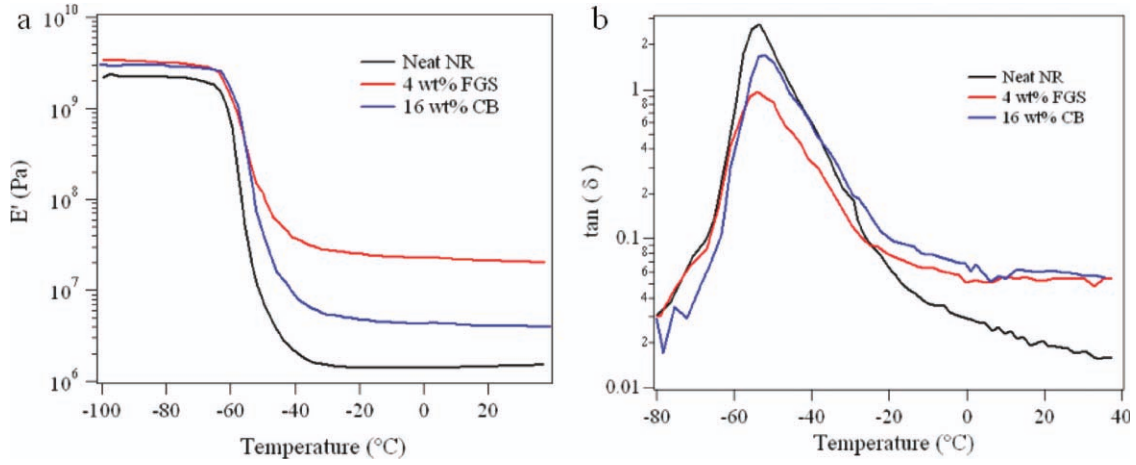

FIGURE 3 Dynamic mechanical data for neat-NR and 4 wt % FGS and 16 wt % CB-filled NR. (a) E' and (b) tan δ versus temperature.

transition of NR, these differences are greatly attenuated.[13] At −80 °C, the E' values for 16 wt % CB and 4 wt % FGS are similar, ~50% larger than E' of neat NR. This observation can be explained by the relative stiffness of the filler (~1 TPa) and the matrix in rubbery (~1 MPa) and glassy phases (~1 GPa).[36,37] Above the glass transition temperature, the stiffness of the composite is mainly affected by the slow dynamics of the immobilized rubber layer and the stress transfer between filler particles. Even at four times lower volume fraction, the interfacial area in the FGS sample is twice that in the CB sample. The onset of strain-induced crystallization (strain amplification) for FGS suggests that small contact regions between crumpled FGS sheets contribute substantially to stress transmission. Linear viscoelastic measurements at low strain do not initiate strain amplification. However, at high strains, strain amplification combines with the effect of immobilized rubber to give the 30- to 90-fold increases in the effective volume fraction discussed above. Below the glass transition temperature (T_g), the distinction between immobilized and free (mobile) rubber disappears, and the difference in the moduli between CB- and FGS-filled rubber becomes small. For FGS, this corresponds to a dramatic decrease in the effective volume fraction for the reinforcing regions from $\phi' = 0.67$ to 0.02.

T_g is not substantially shifted by the addition of either FGS or CB, in contrast to the dramatic increases of 30–40 °C for poly(methyl methacrylate) and poly(acrylonitrile) filled with FGS that we have observed previously.[38] The loss tangent (tan δ) peak positions for neat NR, 4 wt % FGS-NR, and 16 wt % CB-NR samples are within 2 °C of each other. Differential scanning calorimetry experiments on both crosslinked and uncrosslinked samples also show negligible T_g shifts with filler loading (data not shown). We have observed similar behavior in FGS-filled SBR composites as well. Interestingly, the NR composites containing 16 wt % CB and 4 wt % FGS have similar tan δ values at room temperature, although the latter has significantly higher modulus. From this, we conclude that the free chains control T_g for FGS-NR composites and that the free chain dynamics are essentially the same for neat, CB-filled, and FGS-filled NR.

CONCLUSIONS

Simultaneous mechanical and X-ray scattering (WAXD and SAXS) measurements allow us to formulate a picture of the effect of FGSs on crystallization of NR. Neither mechanical nor scattering measurements alone provide adequate data to draw conclusions about the potential roles of strain amplification or immobilized rubber. The comparison of CB-NR and FGS-NR composites provides additional insight and a benchmark for the properties of FGS-NR-filled elastomers. In uniaxial extension at high strains ($0 < \varepsilon < 5$), the stress–strain profiles of 1 wt % FGS correspond to that of 16 wt % CB, with the FGS having a 40% higher ultimate strength and a 16% higher ultimate strain. Using the model of Poompradub et al. as applied to the strain for the onset of crystallization, we find that the effective volume fraction of CB is roughly twice the actual volume fraction, whereas for FGS the effective volume fraction is from 30 to 90 times the actual volume fraction. The high aspect ratio of the FGS sheets, on the order of 400, and crumpled conformation leads to this high effective volume fraction and strain amplification.

The WAXD measurements show a dramatically different behavior for strain-induced crystallization and reinforcement by FGS as compared to CB. The onset of crystallization occurs at much lower stains for FGS-filled NR than for neat or CB-filled NR. With FGS, the crystallites are more strongly oriented by stretching than in CB-filled NR. For NR, CB-filled NR, and FGS-filled NR, the amount of crystallinity just before failure, ~11%, is essentially identical. SAXS measurements show that the FGS sheets are oriented and deformed under extension, whereas anisotropy is not observed for CB. The orientation is reversible for FGS under cyclic strain.

These results suggest the importance of further studies to measure the fractal nature of FGS sheets in the composites and to understand the mechanisms of stress transmission at a more local level. In addition, mechanisms of fatigue and fracture of FGS nanocomposites are unexplored and will be important for many applications. The enhanced mechanical properties that FGS imparts to NR and SBR coupled with its ability to act as a barrier and conductive filler opens up intriguing new applications such as fuel-efficient tires and improved rubber formulations for vibration and noise dampening.

EXPERIMENTAL

Formation of FGSs

FGSs were produced by a two-stage process: oxidation of natural flake graphite into graphite oxide (GO) in a mixture of sulfuric acid, nitric acid, and potassium chlorate followed by exfoliation of GO into graphene sheets by rapid heating (2000 °C/min) to 1050 °C.[4] The absence of graphite and GO X-ray diffraction peaks in the final product indicated a lack of residual stacking. The predominantly single-sheet graphene had a surface area between 500 and 700 m^2/g as measured by nitrogen adsorption and a C/O ratio ~12 by elemental analysis (Atlantic Microlabs). Neat NR, neat SBR, and 20 phr CB-SBR formulations and compounded materials were provided by the Lord (Erie, PA). The formulation consisted of 100 phr rubber, 2 phr sulfur, 1 phr accelerator, 3 phr zinc oxide, 1 phr stearic acid, and 2 phr antioxidants/antiozonant. CB (ASTM -N330) was also supplied by the Lord and was used as it is. Tetrahydrofuran (THF), containing 250 ppm butylated hydroxytoluene as inhibitor, was purchased from Sigma–Aldrich.

Preparation of Composites

Rubber-FGS nanocomposites were prepared by solution processing. Rubber formulations (4 g) were completely dissolved in 100 mL of THF with the aid of a magnetic stirring bar. Then, the required amount of FGS suspended in 10 mL of THF was added to the rubber solution with stirring. After mixing the FGS–rubber–THF solution for an hour with a stir bar, THF was removed by evaporation at room temperature and pressure. Before vulcanization, the samples were left

overnight in a vacuum oven at room temperature to remove the residual THF. Control tensile test experiments were performed to ensure that the mechanical properties of the formulated rubber samples were not affected by solution processing. CB-NR samples at 16 wt % (20 phr) were prepared using a Haake Mini-Lab twin screw extruder (Thermo Electron) with counter-rotating screws at 200 rpm for 0.5 h. The temperature of the extruder was kept at 90 °C to avoid vulcanization of the rubber during the mixing process. NR and SBR samples were vulcanized into 0.5-mm thick films in a phr hot press at 150 °C for 20 min or 165 °C for 30 min, respectively.

Instrumental Analysis

WAXD and SAXS experiments were carried out at the X27C beamline in the National Synchrotron Light Source, Brookhaven National Laboratory. Data are presented against the magnitude of the momentum transfer vector $q \equiv (4\pi/\lambda)\sin\theta$, where λ is the wavelength of the X-ray beam (0.1371 nm), and θ is half the scattering angle. The 2D patterns were collected on a MAR-CCD (MAR USA) detector. The sample-to-detector distances were calibrated using Al_2O_3 and silver behenate standards for wide and small angle scattering, respectively. For both WAXD and SAXS experiments, a 10-mm/min deformation rate was used in tensile tests with ASTM D1708 dogbones. Dynamic mechanical tests were performed with an RSA-III rheometer (TA Instruments, Wilmington, DE) in tension. Temperature sweep experiments were performed between −90 and 40 °C at constant 0.01% strain and 6 rad/s frequency. The samples were first rapidly cooled from room temperature to −100 °C, and the measurements were performed while heating at 10 °C/min.

ACKNOWLEDGMENTS

The authors acknowledge the support of the National Science Foundation MRSEC Program through the Princeton Center for Complex Materials award numbers DMR-0213706 and DMR-0819860. The authors like thank the Lord Corporation for their generous donation of rubber samples used in these investigations.

REFERENCES AND NOTES

1 Donnet, J. B.; Bansal, R. C.; Wang, M. J. Carbon Black, 2nd ed.; Marcel Dekkker Inc: New York, **1993**.

2 Kohjiya, S.; Kato, A.; Ikeda, Y. *Prog. Polym. Sci.* **2008,** *33*, 979–997.

3 Schniepp, H. C.; McAllister, M. J.; Sai, H.; Herrera-Alonso, M.; Adamson, D. H.; Prud'homme, R. K.; Car, R.; Saville, D. A.; Aksay, I. A. *J. Phys. Chem. B.* **2006,** *110*, 8535–8539.

4 McAllister, M. J.; Luen, J.-L.; Adamson, D. H.; Schniepp, H. C.; Abdala, A. A.; Lui, J.; Herrera-Alonso, M.; Milius, D. L.; Car, R.; Prud'homme, R. K.; Aksay, I. A. *Chem. Mater.* **2007,** *19*, 4396–4404.

5 Kim, H.; Abdala, A. A.; Macosko, C. W. *Macromolecules* **2010,** *43*, 6515–6530.

6 Potts, J. R.; Dreyer, D. R.; Bielawski, C. W.; Ruoff, R. S. *Polymer* **2011,** *52*, 5–25.

7 Zhan, Y.; Wu, J.; Xia, H.; Yan, N.; Fei, G.; Yuan, G. *Macromol. Mater. Eng.* **2011,** *296*, 590–602.

8 Bergstrom, J. S.; Boyce, M. C. *Rubber Chem. Technol.* **1999,** *72*, 633–656.

9 Fukahori, Y. *Rubber Chem. Technol.* **2003,** *76*, 548–566.

10 Rezende, C. A.; Bragança, F. C.; Doi, T. R.; Lee, L.-T.; Galembeck, F.; Boué, F. *Polymer* **2010,** *51*, 3644–3652.

11 Lerf, A.; He, H. Y.; Forster, M.; Klinowski, J. *J. Phys. Chem.* **1998,** *102*, 4477–4482.

12 Lerf, A.; He, H. Y.; Riedl, T.; Forster, M.; Klinowski, J. *Solid State Ionics* **1997,** *101*, 857–862.

13 Gent, A. N.; Zhang, L. Q. *Rubber Chem. Technol.* **2002,** *75*, 923–933.

14 Smith, T. L. *Polym. Eng. Sci.* **1977,** *17*, 129–143.

15 Taylor, G. R.; Darin, S. R. *J. Polym. Sci.* **1955,** *17*, 511–525.

16 Gent, A. N.; Kawahara, S.; Zhao, J. *Rubber Chem. Technol.* **1998,** *71*, 668–678.

17 Gonzalez, L.; Valentin, J. L.; Fernandez-Torres, A.; Rodriguez, A.; Marcos-Fernandez, A. *J. Appl. Polym. Sci.* **2005,** *98*, 1219–1223.

18 Rault, J.; Marchal, J.; Judeinstein, P.; Albouy, P. A. *Eur. Phys. J. E* **2006,** *21*, 243–261.

19 Tosaka, M.; Murakami, S.; Poompradub, S.; Kohjiya, S.; Ikeda, Y.; Toki, S.; Sics, I.; Hsiao, B. S. *Macromolecules* **2004,** *37*, 3299–3309.

20 Toki, S.; Sics, I.; Ran, S. F.; Liu, L. Z.; Hsian, B. S.; Murakami, S.; Senoo, K.; Kohjiya, S. *Macromolecules* **2002,** *35*, 6578–6584.

21 Toki, S.; Takagi, R.; Ito, M.; Hsiao, B. S. *Polymer* **2011,** *52*, 2453–2459.

22 Poompradub, S.; Tosaka, M.; Kohjiya, S.; Ikeda, Y.; Toki, S.; Sics, I.; Hsiao, B. S. *J. Appl. Phys.* **2005,** *97*, 103529(9).

23 Kenny, J. C.; BcBriety, V. J.; Rigbi, Z.; Douglass, D. C. *Macromolecules* **1991,** *24*, 436–443.

24 Manna, A. K.; De, P. P.; Tripathy, D. K.; De, S. K.; Chatterjee, M. K. *Rubber Chem. Technol.* **1997,** *70*, 624–633.

25 Bandyopadhyay, S.; De, P. P.; Tripathy, D. K.; De, S. K. *Polymer* **1996,** *37*, 353–357.

26 Roychoudhury, A.; De, P. P. *J. Appl. Polym. Sci.* **1995,** *55*, 9–15.

27 Leblanc, J. L. *J. Appl. Polym. Sci.* **1997,** *66*, 2257–2268.

28 Sheng, E.; Sutherland, I.; Bradley, R. H.; Freakley, P. K. *Eur. Polym. J.* **1996,** *32*, 35–41.

29 Meissner, B. *Rubber Chem. Technol.* **1995,** *68*, 297–310.

30 Wolff, S.; Wang, M. J.; Tan, E. H. *Rubber Chem. Technol.* **1993,** *66*, 163–177.

31 Tosaka, M.; Senoo, K.; Kohjiya, S.; Ikeda, Y. *J. Appl. Phys.* **2007,** *101*, 084909(8).

32 Hernández, M.; LoÇpez-Manchado, M. A.; Sanz, A.; Nogales, A.; Ezquerra, T. A. *Macromolecules* **2011,** *44*, 6574–6580.

33 Trabelsi, S.; Albouy, P. A.; Rault, J. *Macromolecules* **2003,** *36*, 9033–9099.

34 Bokaoza, L. *Macromol. Symp.* **2001,** *169*, 243–260.

35 Zhang, H. P.; Niemczura, J.; Dennis, G.; Ravi-Chandar, K.; Marder, M. *Phys. Rev. Lett.* **2009,** *102*, 245503(4).

36 Halpin, J. C.; Kardos, J. L. *Polym. Eng. Sci.* **1976,** *16*, 344–352.

37 Mori, T.; Tanaka, K. *Acta Metall. Mater.* **1973,** *21*, 571–574.

38 Ramanathan, T.; Abdala, A. A.; Stankovich, S.; Dikin, D. A.; Herrera-Alonso, M.; Piner, R. D.; Adamson, D. H.; Schneipp, H. C.; Chen, X.; Ruoff, R. S.; Nguyen, S. T.; Aksay, I. A.; Prud'homme, R. K.; Brinson, L. C. *Nat. Nanotechnol.* **2008,** *3*, 327–331.